

E2838

Fig. 17.13

Comparison of the energy in superhot electrons and 3/2-harmonic emission. The remarkable similarity in the curves strongly suggests that the superhot electrons are produced by the $2\omega_p$ instability.

ACKNOWLEDGMENT

This work was supported by the U.S. Department of Energy Office of Inertial Fusion under contract number DE-AC08-80DP40124 and by the Laser Fusion Feasibility Project at the Laboratory for Laser Energetics which has the following sponsors: Empire State Electric Energy Research Corporation, General Electric Company, New York State Energy Research and Development Authority, Northeast Utilities Service Company, The Standard Oil Company, and University of Rochester. Such support does not imply endorsement of the content by any of the above parties.

REFERENCES

1. W. Seka, R. S. Craxton, J. Delettrez, L. M. Goldman, R. Keck, R. L. McCrory, D. Shvarts, J. M. Soures, and R. Boni, *Opt. Commun.* **40**, 437 (1982).
2. LLE Review 13, 23 (1982).

2.B Parametric Instabilities in Underdense Spherical Plasmas with $\lambda=351$ nm Illumination

The six-beam ultraviolet OMEGA coronal physics program is motivated by the fact that all energy input to laser-fusion targets occurs within the coronal plasma. In this region, the bulk of the laser energy is absorbed through inverse-bremsstrahlung (collisional) absorption. The coronal plasma, heated to temperatures of 1 to 3 keV, expands into the vacuum and by reaction compresses the core of the target. A very high compression is essential for the success of laser fusion, and the quality of the compression depends critically on many parameters in the plasma corona.

Laser light of frequency ω_0 incident on a spherical target is absorbed on its way to the critical-density surface mostly by collisional absorption. A small part of the incident energy is also channeled into a host of parametric instabilities,² most notably the $2\omega_p$ decay instability at the quarter-critical ($n_e = n_c/4$) surface, where laser photons decay into plasmon (plasma-wave) pairs of frequency $\omega \approx \omega_0/2$, which is the local plasma frequency of the quarter-critical surface. This region then becomes a source of energetic electrons (superhot electrons), as well as a number of half-integer harmonics of the incident laser light ($\omega_0/2, 3\omega_0/2, 5\omega_0/2$, etc.).

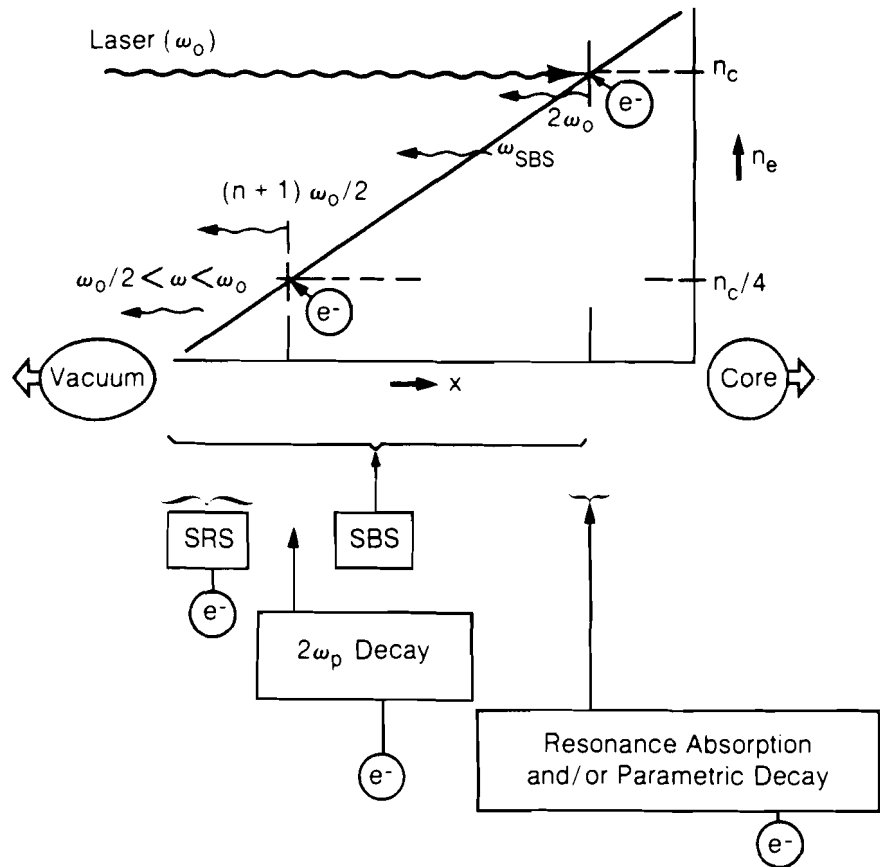
Light penetrating up to the critical-density ($n_e = n_c$) surface can be absorbed in that region through resonance absorption. This process is dominant for long-wavelength irradiation, but for 351-nm irradiation at pulse lengths longer than 100 ps, no evidence for resonance absorption has been found.¹

Until recently, most UV-laser-plasma interaction experiments were carried out with a single beam incident on flat targets. A large data base has been collected, and most diagnostics indicate a strongly two-dimensional (2-D) behavior of these plasmas. In particular, self-focusing of the laser light is found to abound under these conditions at incident intensities above 5×10^{13} W/cm².³⁻⁷ In contrast, uniformly illuminated spherical targets are expected to exhibit a much more one-dimensional (1-D) character allowing for much easier interpretation of many of the plasma-physics effects occurring in the corona.

The diagnostics used in these experiments are mostly optical and x-ray spectroscopy. The latter serves as an energetic-electron monitor, while the former can give detailed information on the specific parametric processes occurring in the corona. Furthermore, these visible spectra can serve as a valuable coronal diagnostic for the electron temperature at various locations in the plasma.

A schematic coronal electron-density profile is shown in Fig. 17.14, along with the various parametric processes and their ramifications, in terms of hot-electron generation and optical signatures. The critical-density processes like resonance absorption and parametric decay are seen clearly in OMEGA infrared experiments through careful analysis of the $2\omega_0$ and x-ray spectra from these plasmas.⁸ So far, we have been unable to investigate any $2\omega_0$ spectra in our UV experiments, but the continuum hard x-ray spectra show no evidence for resonance absorption.

The $2\omega_p$ decay instability at $n_c/4$ is observed both in its optical signals and in the x-ray signature of the superhot electrons generated by this instability. Evidence for stimulated Brillouin scattering (SBS), an instability in which the incident laser light decays into an ion-acoustic wave and an electromagnetic wave,⁴ is found in the highest-intensity OMEGA shots only. However, the SBS levels observed even in these cases are negligibly small. Most recently, optical spectra have been observed on OMEGA which have traditionally been attributed to stimulated Raman scattering (SRS) below $n_c/4$, where an incident

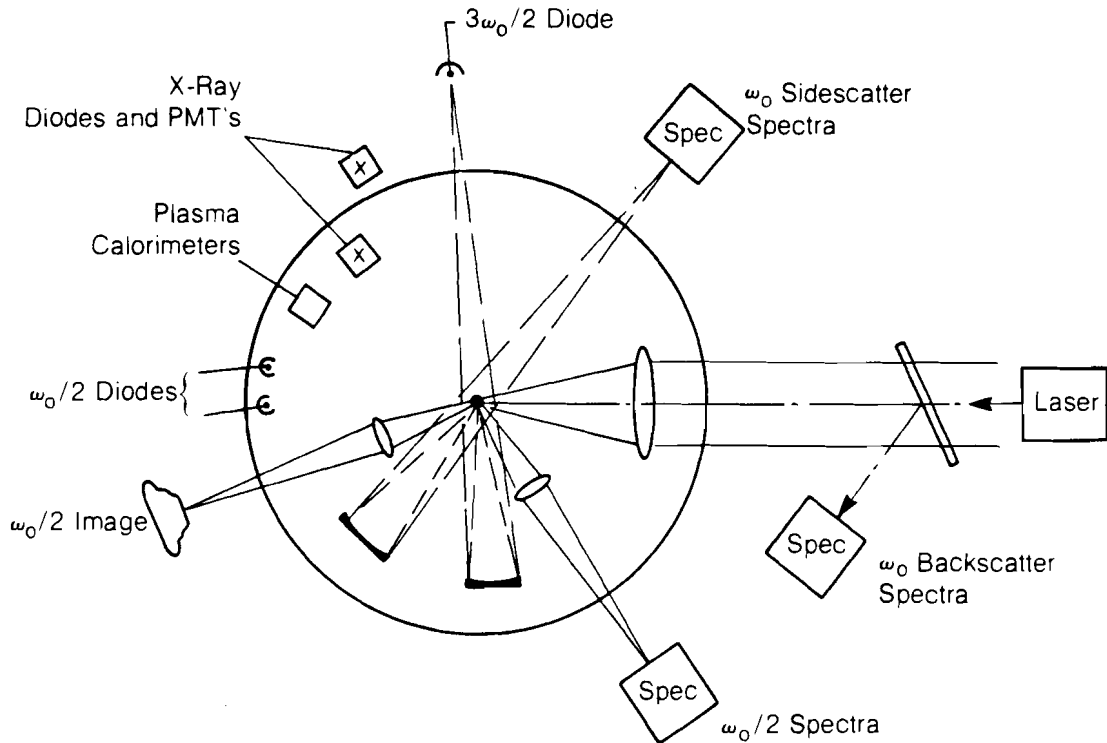


E2615

Fig. 17.14
Schematic plot of the coronal electron density profile showing where the various parametric processes occur. The plot shows the characteristic electromagnetic signals generated by the parametric process labelled beneath the plot. The generation of energetic electrons, chiefly through the damping of electron plasma waves, is indicated by a circled "e."

photon decays into a plasmon and a scattered photon, but from threshold considerations, this instability should not be excited at intensities below 10^{15} W/cm² where the experiments were conducted. We are presently studying these spectra as well as novel theoretical models for their interpretation.

Figure 17.15 is a schematic layout of the coronal diagnostics employed in the new multibeam experiments. The light scattered by the target near the fundamental irradiation frequency ω_0 is analyzed spectroscopically in backscattering and sidescattering. Another spectrometer analyzes the $\omega_0/2$ radiation. Photodiodes with appropriate filters have been absolutely calibrated to measure the light energy scattered at $\omega_0/2$ and $3\omega_0/2$. A camera filtered to photograph the target in the scattered light at $\omega_0/2$ is used to investigate the $\omega_0/2$ emission pattern. X-ray diodes and photomultipliers are used to measure the x-ray continuum spectrum between 2 and 200 keV. Plasma calorimeters are used to measure the amount of laser light absorbed by the plasma.



DIAGNOSTICS:

- ω_0 backscatter and sidescatter spectroscopy
- $\omega_0/2$ spectroscopy, diodes, image
- $3\omega_0/2$ diodes
- X-ray diodes and photo-multiplier tubes (PMT's)
- Plasma calorimeters

E2749

Fig. 17.15
Schematic lay-out of diagnostics used in the coronal physics experiments on OMEGA. The spectroscopic diagnostics cover wavelengths from the IR to the hard x-ray region. Reflective optics with dielectric coatings were used for imaging and/or light collection between 200 and 400 nm for ease of alignment and optimum light-gathering efficiency.

Threshold formulae and typical threshold intensities for our UV interaction experiments are shown in Fig. 17.16. While the threshold condition for SBS should be surpassed in most of our OMEGA shots, we have not seen SBS, except in the highest-intensity shots. This is consistent with experiments done elsewhere. The reason for the absence of SBS is not completely clear at this point. The filamentation threshold depends on a number of factors, particularly the degree of uniformity of irradiation. For uniform OMEGA irradiation, the filamentation threshold may be considerably higher than the range of values indicated in this figure. The $2\omega_p$ instability has indeed been found to have a threshold near 2×10^{14} W/cm².

- Predicted and Observed Thresholds of Parametric Instabilities -

| | Theory W/cm^2 | Typical Prediction W/cm^2 | Observed W/cm^2 |
|---------------------|--|-----------------------------------|----------------------|
| • $2\omega_p$ Decay | $\frac{5 \times 10^{12} T_{eV}}{L_{\mu m} \lambda_{\mu m}}$ | 2×10^{14} | 6×10^{13} |
| • SRS-Absolute | $\frac{5 \times 10^{17}}{L_{\mu m}^{3/4} \lambda_{\mu m}^{2/3}}$ | 3×10^{15} | 4×10^{14} |
| • SRS-Convective | $\frac{4 \times 10^{17}}{L_{\mu m} \lambda_{\mu m}}$ | 2×10^{16} | 4×10^{14} |
| • SBS | $\frac{4 \times 10^{11} T_{eV}}{L_{\mu m} (n_e/n_c)}$ | 2×10^{13} | 6×10^{13} |
| • Filamentation | | $1-3 \times 10^{14}$ | 10^{14} |
| • Parametric Decay | $\frac{7 \times 10^{11} T_{eV}}{L_{\mu m} \lambda_{\mu m}}$ | 2×10^{14} | 10^{14} |

Typical predictions for: $\lambda = 351$ nm, $L = 75$ μm at $n_c/4$, $L = 10$ μm at n_c ,
 $T = 1$ keV

E2624

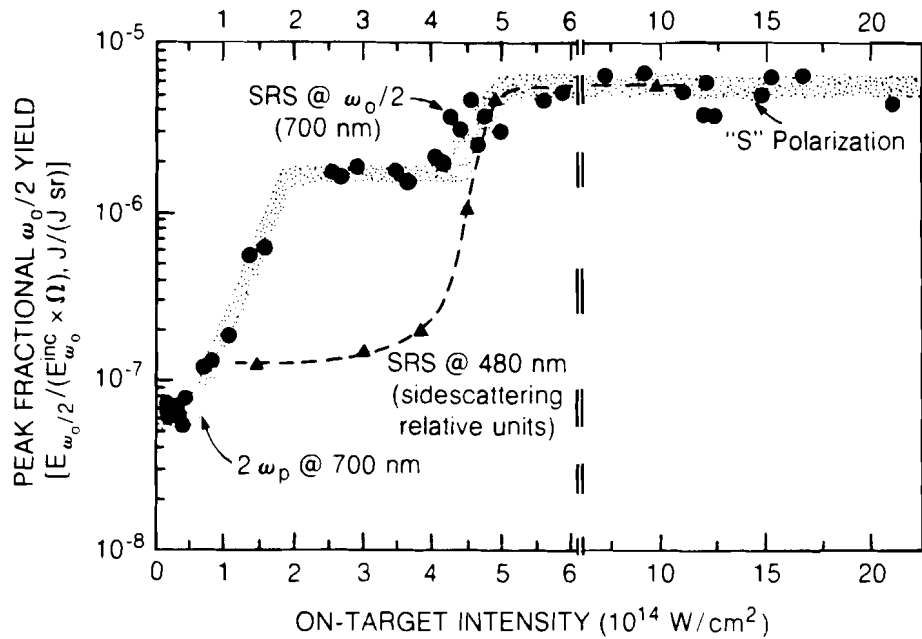
Fig. 17.16

List of parametric instabilities, their theoretical threshold formulae, and typical theoretical predictions along with experimental thresholds observed in single-beam GDL experiments. While scale lengths between 50 and 75 μm are typical near the $n_c/4$ surface for current UV-laser-plasma experiments, scale lengths around 10 μm are expected near the n_c surface and were used to estimate the parametric decay threshold (last entry in the list above).

Earlier Interaction Experiments at LLE

To set the stage for the new OMEGA results, a short review of the old, single-beam experiments is presented in Figs. 17.17 through 17.20. The common thread in these single-beam experiments is the necessity of resorting to filamentation of the laser beam in the corona to explain the many different experimental results.

Figure 17.17 shows single-beam results for light energy scattered at $\omega_o/2$ (700 nm) and at 480 nm, plotted as functions of irradiation intensity.⁸ The former has two steps: the first corresponds to the onset of the $2\omega_p$ instability, and the second corresponds to the absolute SRS instability. The 480-nm signal is related to the convective SRS instability, and it also shows a rapid rise at 4×10^{14} W/cm^2 , even though the theoretical threshold for this process is ten times higher than the absolute SRS threshold. Furthermore, the thresholds observed here for the $2\omega_p$ and absolute SRS are themselves too low by factors of 5 to 10. This discrepancy can be explained only by invoking filamentation, for which there are also other indicators (see below).



E1521

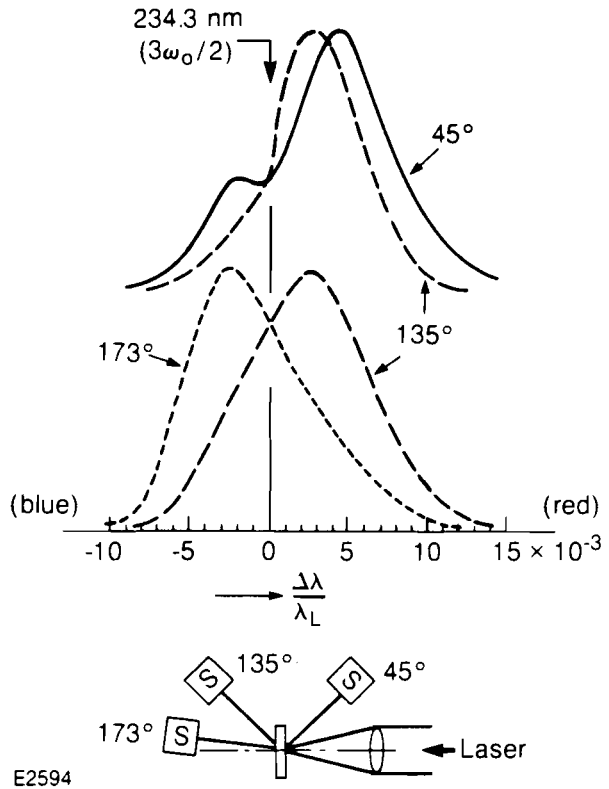
Fig. 17.17
 Light emission from UV-laser plasmas at 700 nm (●) and at 480 nm (▲). Planar CH targets were illuminated with 0.5-ns pulses focused onto spots of varying size (100 to 500 μm). Emission was observed in the same polarization as the incident light. The 700-nm signal at half the laser frequency exhibits two thresholds corresponding to the $2\omega_p$ decay and absolute SRS instability. The 480-nm signal originates from the convective SRS instability and has an observed threshold equal to that of the absolute instability. All thresholds are at variance with those predicted theoretically. Filamentation of the incident laser light in the corona may explain this discrepancy. Note the scale change at 6×10^{14} W/cm².

The $3\omega_c/2$ spectra have frequently been used as a temperature diagnostic for the corona. However, the theories of the upscatter of laser photons by $2\omega_p$ plasmons usually applied cannot begin to account for the complexity of spectra seen in UV, single-beam GDL experiments. Depending on the angle of observation, one sees asymmetric, double-humped spectra or single-line red- or blue-shifted spectra (see Fig. 17.18). The explanation has been found in a detailed analysis of the $2\omega_p$ decay and the $3\omega_c/2$ generation in filaments.⁵

Although the convective SRS threshold is exceedingly high ($\geq 10^6$ W/cm²), we have seen characteristic SRS spectra in single-beam experiments for this instability.⁶ Careful analysis of these SRS spectra has enabled us to determine time-resolved electron temperatures as shown in Fig. 17.19. Compared to the work described in Ref. 5, a more complete SRS theory⁹ is applied here, leading to somewhat different coronal electron temperatures than those deduced earlier. We note that the deduced temperatures lie below 2-D hydrocode predictions. We have attributed this discrepancy to depleted tails in the electron distribution function, as expected from the theory of inverse-bremsstrahlung absorption. The mere existence of the SRS spectra, however, requires the existence of filaments, inside which the requisite intensities may indeed exist along with anomalously long density gradients.

Fig. 17.18

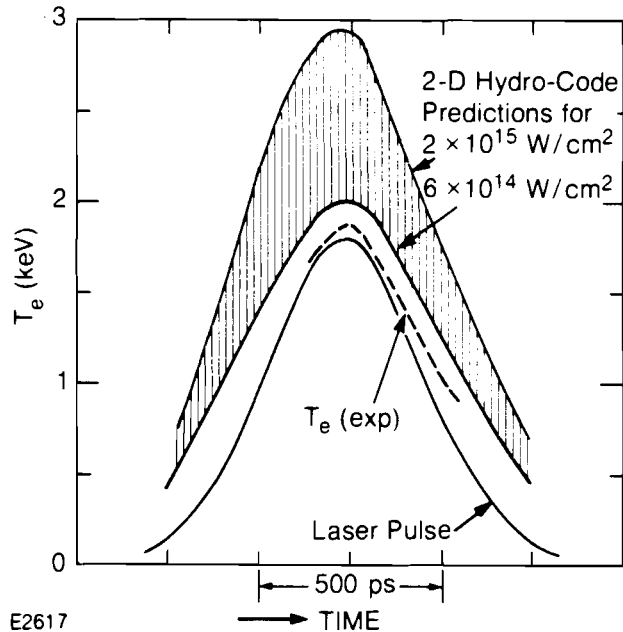
Spectra of the $3\omega_c/2$ emission from thin CH targets for planar 351-nm irradiation. The schematic experimental layout is shown in the lower part of the figure. The various spectra shown refer to different observation angles as indicated. The marked difference between the spectra in the three directions of observation are obvious: they cannot be explained on the basis of the conventional theory of 3/2-harmonic generation. An adequate explanation is given by a model which assumes the $2\omega_b$ decay instability and 3/2-harmonic generation to occur inside self-focusing filaments.



E2594

Fig. 17.19

Time-resolved coronal electron temperatures as determined from streaked SRS spectra obtained from 351-nm, 0.5-ns pulses at 10^{15} W/cm² on planar CH targets. Using a recently developed theory by E. A. Williams for the location of the center of gravity of the convective SRS spectrum as a function of coronal electron temperature, we have plotted experimentally deduced electron temperatures (dashed curve). Also shown in this figure are predicted coronal electron temperatures using the 2-D hydrocode SAGE for two different irradiation intensities (solid curves). We note the close resemblance in shape between experimental and simulated electron temperature evolution. A variety of effects may be responsible for the differences observed in the actual values of the temperatures.

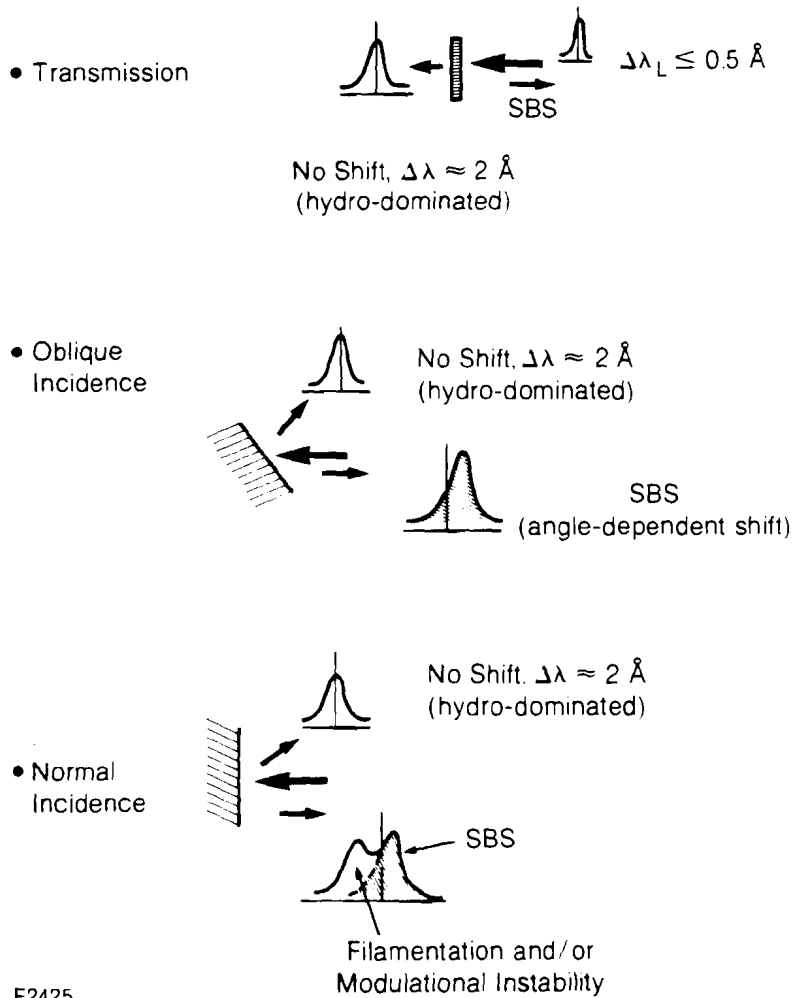


E2617

Fig. 17.20

Schematically depicted spectra of light scattered near the irradiation frequency for single-beam, UV-laser plasmas obtained from planar CH targets. Spectra of transmitted light for thin-target experiments as well as spectra of specularly reflected light in oblique-incidence experiments show little spectral broadening and small or no spectral shifts. This is consistent with shifts and Doppler broadening due to plasma motion. Typical SBS spectra are observed in backscattering from oblique-incidence experiments. At normal incidence, the backscatter spectra are complicated by filamentation effects.

Figure 17.20 depicts schematically the various types of scattered light spectra seen near ω_0 in single-beam experiments.⁴ Starting from the top of the figure, light seen in transmission is generally unshifted from its original frequency and is Doppler-broadened by the hydrodynamic motion of the plasma it traverses. At oblique incidence, SBS backscatter spectra are observed above a threshold near 10^{14} W/cm². The specularly reflected light only suffers slight broadening and negligible shifts, in accordance with expectations for a purely hydro-dominated spectrum. The situation is much more complex at normal incidence. The backscatter spectra show red- and blue-shifted components above a few $\times 10^{14}$ W/cm². Analysis of these spectra has shown that filamentation in the corona can also account for these spectra at normal incidence. This does not mean that filamentation only occurs at normal incidence, but it does imply that the filaments must encounter a critical-density layer for the backscatter spectra to show the strong broadening to the blue side of the incident laser frequency.



E2425

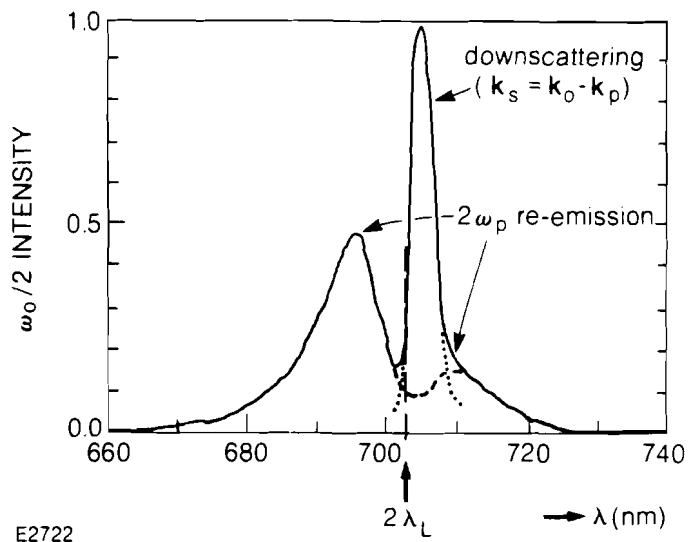
New OMEGA Experiments

The new OMEGA ultraviolet coronal physics results are all characterized by a high degree of reproducibility and an apparent absence of filamentation. At least, none of the experimental data to date require recourse to filamentation to explain their signatures.

The half-harmonic spectrum shown in Fig. 17.21 is typical of a large number of OMEGA shots. Three distinct features are discernible. The dominant sharp line is slightly red-shifted from the $\omega_0/2$ frequency ($2\lambda_L$ wavelength). This line is accompanied by two much broader lines placed approximately symmetrically with respect to $\omega_0/2$. The dashed lines in the figure are drawn to guide the eye. The intensity scaling of all the features as well as the change of the detailed intensity ratios between the various components of the $\omega_0/2$ spectra for different target materials leads us to interpret the spectra in the following way.

The strong, narrow peak is associated with downscattering of the incident photons on the plasmons produced by the $2\omega_p$ decay at $n_c/4$. In this process, the \mathbf{k} -matching conditions, $\mathbf{k}_s = \mathbf{k}_o - \mathbf{k}_p$, have to be fulfilled along with the condition $\omega_s = \omega_o - \omega_p$. Here, \mathbf{k}_o , ω_o and \mathbf{k}_s , ω_s are the wave vectors and frequencies of the incident and scattered electromagnetic wave, and \mathbf{k}_p , ω_p are the wave vector and frequency of the plasma wave. It can be shown from the photon and plasmon dispersion relations that these matching conditions are satisfied for only a very narrow range of \mathbf{k} 's, which leads to the sharp line shown in Fig. 17.21. Furthermore, the red shift of this line is well-defined for the same reason and may be written as $\Delta\lambda = 31 \times T_e \text{ keV}$. This relation is obtained from recent work on the $2\omega_p$ decay instability.^{5,10}

Fig. 17.21
Half-harmonic ($\omega_0/2$) spectra from spherical six-beam, UV-laser plasmas obtained using $4 \times 10^{14} \text{ W/cm}^2$ illumination. A typical, highly reproducible, half-harmonic spectrum obtained on OMEGA using a spherical CH target is shown. The dashed and dotted lines are shown to help distinguish the underlying spectral features. The sharp spike is due to ordinary (non-stimulated) Raman scattering (also down-scattering), while the broad features are due to plasmon-to-photon conversion via inverse resonance absorption.



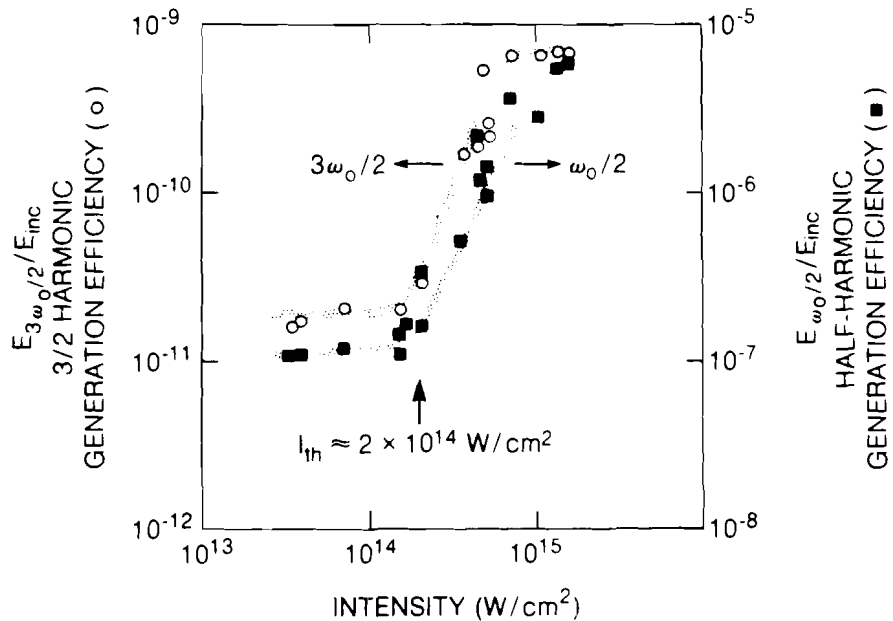
In contrast, the broad $\omega_0/2$ decay features derive from a process which may be termed "inverse resonance absorption." As in resonance absorption, this emission is more efficient for certain plasmon k_p -vectors whose angles with respect to the density gradient coincide with the maximum of the Ginzburg" formula for resonance absorption. Since this maximum is not very sharp, and since the perpendicular component of k_p is directly related to the frequency shift of the plasmon from the center frequency, $\omega_0/2$, we expect broad spectral features whose shifts are sensitive to the density-gradient scale length near $n_c/4$. Indeed, shorter scale lengths produced in high-Z target-irradiation experiments lead to considerably larger displacements to the red and blue of these broad spectral features while affecting the sharp spike only negligibly. It is this effect that has been so disturbing for a long time, since it was in apparent contradiction to the conventional interpretation of these spectra.

Fig. 17.22

Half-integer harmonic emission from spherical UV-laser CH plasmas. The intensity dependence of the $\omega_0/2$ and $3\omega_0/2$ signals indicated by the shaded curves shows the close relationship between the two harmonics. Both involve plasmons generated by the $2\omega_p$ decay at the $n_c/4$ surface, but the exact generation processes are not just upscattering and downscattering (ordinary Raman Stokes and anti-Stokes lines). The apparent saturation of the signals at high intensities could possibly be due to reduced density scale lengths in the corona of the smaller targets used in this intensity regime.

In short, the $\omega_0/2$ spectra contain a sharp feature which promises to be a good coronal temperature diagnostic, along with broad features whose dependence on density gradient, temperature, and incident intensity make them all but useless for coronal temperature diagnostics.

Figure 17.22 shows the intensity dependence of the $\omega_0/2$ and $3\omega_0/2$ conversion efficiencies in low-Z CH targets. The differences of 10^2 in the scales are contrary to expectations for upscattering and downscattering (Stokes and anti-Stokes Raman lines), provided the processes happen in the same region in space. However, the latter is



E2718

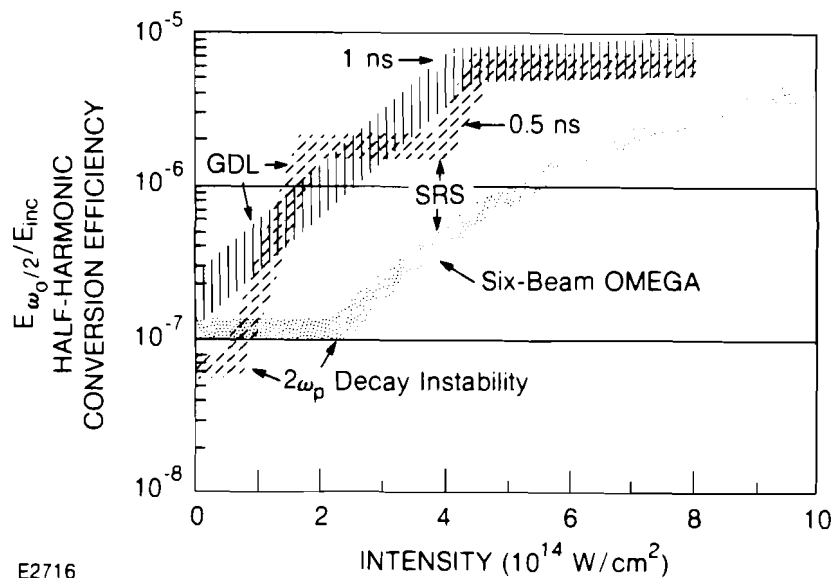
not given *a priori* since detailed analysis of the \mathbf{k} -vector matching conditions shows that the plasma waves must travel some distance in the density gradient in order to acquire the appropriate \mathbf{k} -vector length for $3\omega_0/2$ generation.

The two half-harmonics show a clear threshold at $\sim 2 \times 10^{14}$ W/cm², in good agreement with the theoretically predicted threshold for the $2\omega_p$ decay instability for our experimental conditions. The close resemblance of the two curves reflects their common element, namely, the plasmons produced by the $2\omega_p$ decay instability. The $3/2$ harmonic is produced by the $\mathbf{k}_s = \mathbf{k}_o + \mathbf{k}_p$, $\omega_s = \omega_o + \omega_p$ process, and the $\omega_0/2$ harmonic is produced by the downscattering and/or plasmon-photon conversion described earlier. Both curves appear to saturate around 10^{15} W/cm². The saturation level for the $\omega_0/2$ generation efficiency is slightly less than 10^{-5} , which is exactly the same saturation level as has been observed in the single-beam experiments in GDL.

High-Z targets show similar generation efficiencies, but the $2\omega_p$ decay threshold is approximately twice that for plastic targets. The shorter scale lengths predicted for these plasmas, along with the slightly higher coronal temperatures, are consistent with this difference.

The similar saturation levels of the half-harmonic conversion efficiency for the single-beam, flat-target experiments and the six-beam, spherical-target experiments are shown in Fig. 17.23. We note a much slower rise for the spherical experiments. This can be explained by assuming spatially uniform illumination and by determining how much of the temporal pulse shape lies above threshold. The

Fig. 17.23
Half-harmonic light emission from spherical and planar UV-laser plasmas using CH targets. We note the increased threshold for the $2\omega_p$ decay instability observed in the spherical irradiation experiments. No separate SRS threshold is observed in either the long-pulse (1-ns) planar plasmas or the spherical experiments.

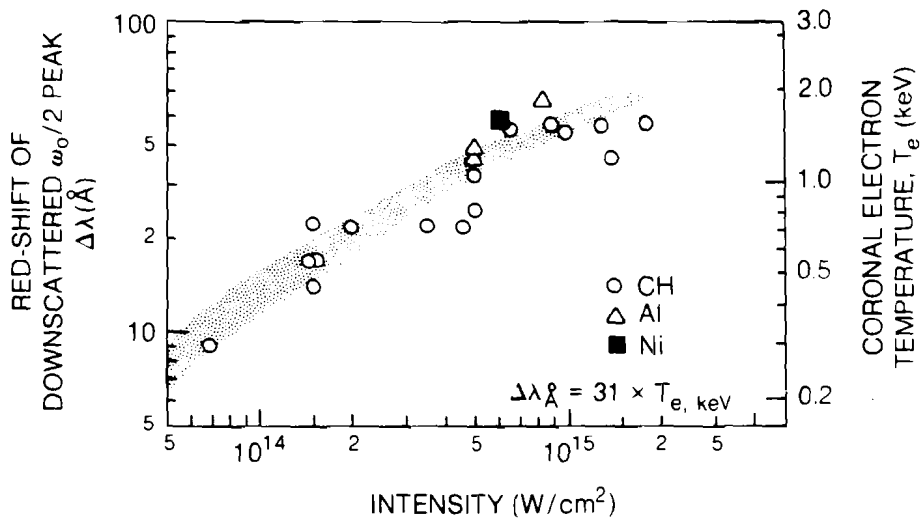


result is an error-function roughly coinciding with the curve shown in Fig. 17.23. The single-beam experiments, in contrast, are filamentation-driven, leading to a different intensity dependence.

The intensity dependence of the red shift of the sharp $\omega_0/2$ feature (Fig. 17.21) is shown in Fig. 17.24. The circles are for CH targets, and the triangles and square are for Al and Ni targets, respectively. On the right-hand side is a coronal temperature scale related to the wavelength-shift scale according to the relation $\Delta = 31 \times T_{e, \text{keV}}$. The coronal temperatures thus deduced are again somewhat lower than those predicted by hydrocode calculations. Part of this difference may be attributed to the possibility that the sharp spectral feature may be more efficiently radiated early during the pulse, before the $2\omega_p$ decay instability has had time to steepen the density profile near the $n_c/4$ surface. At that time, this feature may become weak, if not extinct. It is certainly worth noting that in Fig. 17.19 we arrived at coronal temperatures between 1.5 and 1.8 keV, quite like the temperatures of ~ 1.5 keV indicated in Fig. 17.24 that were deduced for the same incident intensity from time-integrated spectra of the type shown in Fig. 17.21.

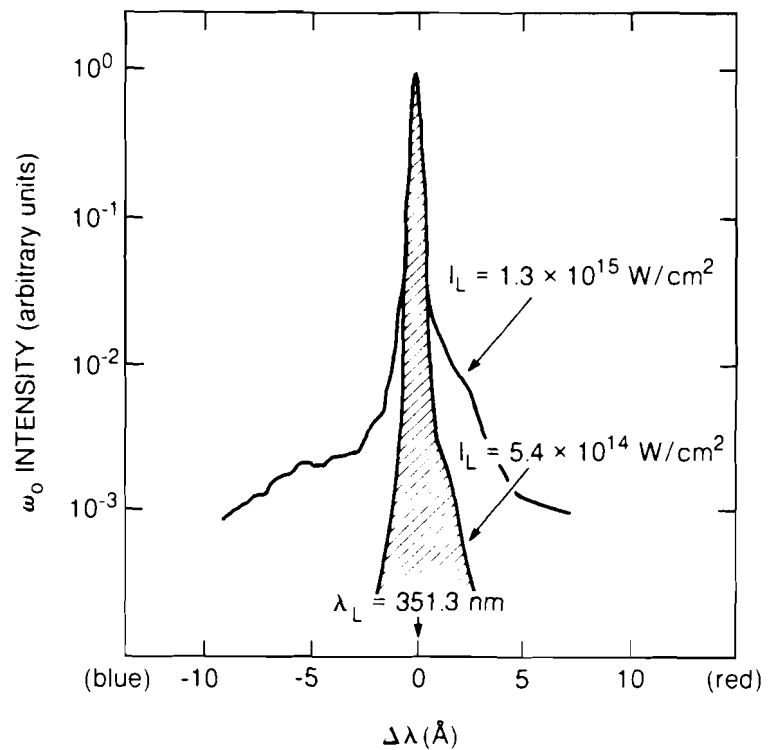
Fig. 17.24

Coronal electron temperatures as obtained from ordinary Raman-scattering (down-scattering) measurements at $\omega_0/2$ with spherical 650-ps UV illumination. The red shift of the sharp feature of the $\omega_0/2$ spectrum (shown in Fig. 17.21) is shown as a function of incident intensity in OMEGA experiments. The intensity-dependent red shift follows roughly the I law suggested by the shaded area. The red shift, $\Delta\lambda$, is related to the coronal electron temperature by $\Delta\lambda = 31 \times T_{e, \text{keV}}$. The temperatures thus determined lie somewhat below 2-D hydrocode predictions.



E2724

Figures 17.25 and 17.26 are spectra of the scattered light near the fundamental frequency in backscattering. Figure 17.25 shows the generally narrow backscatter spectra observed in these experiments. The highest-intensity shots under uniform illumination conditions show a weak but discernible red wing which may be attributed to SBS. In contrast, two shots taken at the same irradiation intensity, but for different focusing conditions, show dramatically different spectra as shown in Fig. 17.26. The surface-focus spectra exhibit exactly the same broad spectra seen in single-beam experiments at normal



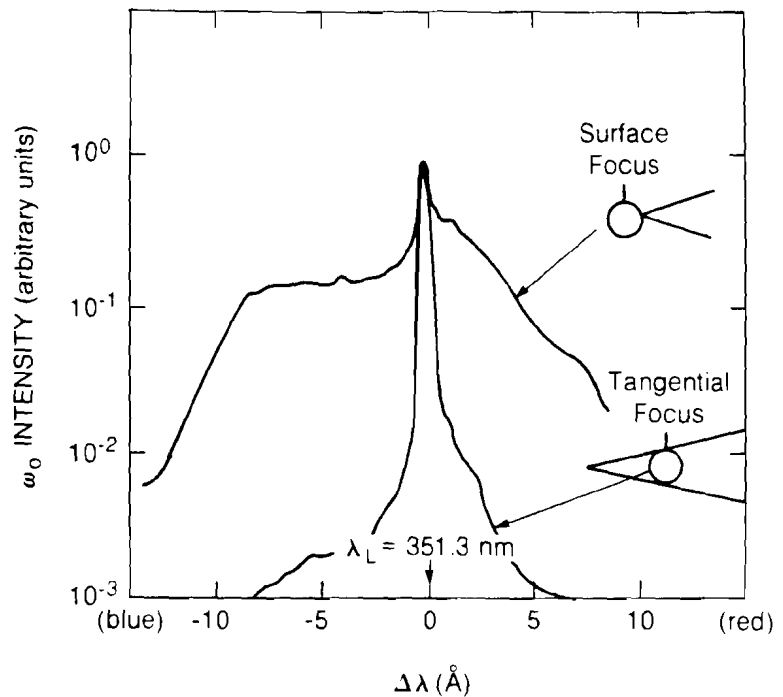
E2748

Fig. 17.25
Backscatter spectra at ω_0 from uniformly illuminated (at tangential focus), UV-laser plasmas using spherical CH targets and 0.6-ns pulses. Note the wide dynamic range obtained in these experiments. The principal feature is only Doppler broadened. At the highest accessible intensities, a small, red-shifted SBS component is observed.

incidence. Indeed, the surface-focus experiments may be viewed as six, single-beam experiments at normal incidence. We thus see the dramatic difference between uniform spherical illumination and single-beam experiments. The latter are dominated by self-focusing (filamentation), while the former apparently exhibit a well-behaved 1-D character.

Summary

The OMEGA coronal physics experiments show much-improved coronal plasma conditions, compared to single-beam experiments. Notably, the apparent absence of filamentation of the incident laser light in the corona creates more benign plasma conditions where thresholds for the $2\omega_0$ decay instability now agree with theoretical predictions, and the signatures of this instability, namely the half-harmonic spectra, can now be said to be reasonably understood (3/2-harmonic spectra have not yet been taken). This understanding has enabled us to use one of the $\omega_0/2$ spectral features as a convenient electron-temperature diagnostic. In addition, the presence of very weak SBS radiation has been established at the highest irradiation intensities ($\geq 10^{15}$ W/cm²) in OMEGA. The high quality of the data and their reproducibility have led to an increased understanding of the plasma physics, while not uncovering any unexpected detrimental effects for direct-drive laser fusion.



E2746

Fig. 17.26

Backscatter spectra at ω_0 from spherical UV-laser plasmas using CH targets and different illumination conditions at constant irradiation intensities (1.3×10^{13} W/cm², $t_L = 0.6$ ns). The strongly broadened (red- and blue-shifted) spectra for surface-focused illumination starkly contrast the spectra for tangentially focused, uniform illumination. The former are consistent with earlier single-beam experiments.

ACKNOWLEDGMENT

This work was supported by the U.S. Department of Energy Office of Inertial Fusion under contract number DE-AC08-80DP40124 and by the Laser Fusion Feasibility Project at the Laboratory for Laser Energetics which has the following sponsors: Empire State Electric Energy Research Corporation, General Electric Company, New York State Energy Research and Development Authority, Northeast Utilities Service Company, The Standard Oil Company, and University of Rochester. Such support does not imply endorsement of the content by any of the above parties.

REFERENCES

1. W. Seka, R. S. Craxton, J. Delettrez, L. M. Goldman, R. Keck, R. L. McCrory, D. Shvartz, J. M. Soures, and R. Boni, *Opt. Commun.* **40**, 437 (1982).
2. W. L. Kruer, *Comments Plasma Phys. and Controlled Fusion* **6**, 167 (1981); C. E. Max, Lawrence Livermore National Laboratory Report UCRL-53107, 1982; M. N. Rosenbluth, *Phys. Rev. Lett.* **29**, 565 (1972); C. S. Liu in *Advances in Plasma Physics*, edited by A. Simon and W. B. Thompson (Wiley, New York, 1976), Vol. 6, p. 121.
3. R. W. Short, R. Bingham, and E. A. Williams, *Phys. Fluids* **25**, 2302 (1982); R. Bingham and C. N. Lashmore-Davies, *Nucl. Fusion* **16**, 67 (1976); O. Willi and P. T. Rumsby, *Opt. Commun.* **37**, 45 (1981); H. A. Baldis and P. B. Corkum, *Phys. Rev. Lett.* **45**, 1260 (1980).